Dalton Transactions

ROYAL SOCIETY OF CHEMISTRY

PAPER

View Article Online
View Journal | View Issue

Cite this: *Dalton Trans.*, 2025, **54**, 8461

The role of manganese oxidation states in the performance of SiC-supported composites toward SF_6 degradation†

Yaru Zhang,‡[a] Xiang Meng,‡[a] Boxu Dong,[a] Fengxiang Ma,[b] Yue Zhao,[b] Xinhua He,*[a] Shan Zhu*[b] and Jiantao Zai *[a]

Received 24th March 2025,
Accepted 23rd April 2025

DOI: 10.1039/d5dt00714c

rsc.li/dalton

Sulfur hexafluoride (SF_6) is a potent greenhouse gas with a significant impact on the environment and there is a need to develop effective strategies toward its degradation. In this study, a series of composites with Mn-based metal active centers were synthesized using a simple and efficient milling method with SiC as the carrier to determine the effect of different oxidation states of Mn on SF_6 degradation. The results showed that the performance of Mn-based composites with different oxidation states in the degradation of SF_6 had an obvious hierarchy: SiC–Mn(0) > SiC–MnO(II) > SiC–Mn_2O_3(III) > SiC–MnO_2(IV). Among them, SiC–Mn composites with Mn monomers as active centers reach a degradation capacity of 62.27 mL g^{-1} at 600 °C. This performance trend is attributed to the stronger electron-supplying ability of the Mn species with lower valency, which enhances the cleavage of the strong S–F bonds in SF_6. This study emphasizes the importance of Mn oxidation states in determining the catalytic efficiency of Mn-based composites for SF_6 degradation.

1. Introduction

Fluorinated pollutants, due to their exceptional chemical stability and persistence in the environment, have become an increasing environmental concern and have significantly exacerbated the global warming crisis.[1,2] These pollutants, including hydrofluorocarbons (HFCs), perfluorocarbons (PFCs), and sulfur hexafluoride (SF_6), contribute not only to climate change but also to long-term environmental pollution.[3,4] Among these gases, SF_6 has the greatest greenhouse effect, with a 100-year global warming potential (GWP) of 25 200 times that of CO_2.[5] In recent years, SF_6 has been widely used in electrical grids for its excellent electrical insulation and arc-quenching properties, resulting in a rapid increase in emissions.[6,7] Therefore, controlling SF_6 emissions is essential to mitigate its impact on global warming.

High concentrations of SF_6 (above 70%) are usually recovered by distillation purification.[8] However, purification of low concentrations of SF_6 is more challenging. Adsorption and degradation are commonly used to reduce emissions of low concentrations of SF_6, but adsorption removes only a small fraction of SF_6 and involves complex post-treatment processes.[9,10] In contrast, degradation is the most promising strategy for the complete elimination of SF_6. Currently, the treatment technologies for SF_6 are mainly focused on high-temperature pyrolysis, photocatalytic reduction, plasma decomposition and thermocatalytic degradation.[11,12] High-temperature pyrolysis decomposes SF_6 by exposing it to high temperatures above 1000 °C, but this method consumes much energy and is prone to produce harmful by-products. Photocatalytic reduction degrades SF_6 using ultraviolet light and reactive intermediates produced by organic reductants, and despite its relatively low energy consumption, its degradation efficiency is insufficient to meet demands of commercialization. Plasma technology generates high-energy particles to decompose SF_6 through high-voltage electric fields, but the equipment is complicated and costly. Thermal catalytic degradation technology is able to completely decompose SF_6 using catalysts at temperatures of 600–800 °C, and is considered to be the most promising technology for harmless treatment of SF_6.[13] For example, Zhang *et al.* utilized stainless steel slag (SSS) to efficiently degrade SF_6 for 150 min at a reaction temperature of 700 °C and a gas flow rate of 13.4 mL min^{-1} with a degradation capacity as high as 3.86 mL g^{-1}, and even at 500 °C, the SF_6 degradation capacity of this SSS material could

[a]*Shaoxing Research Institute of Renewable Energy and Molecular Engineering, Shanghai Jiao Tong University, Shaoxing, 312000, China. E-mail: xinhuahe@sjtu.edu.cn, zaijiantao@sjtu.edu.cn*
[b]*Electric Power Research Institute, State Grid Anhui Electric Power Co., Ltd, Hefei, 230601, China. E-mail: shanzhu@mail.ustc.edu.cn*

†Electronic supplementary information (ESI) available. See DOI: https://doi.org/10.1039/d5dt00714c

‡These authors contributed equally to this work.

reach 1.52 mL g^{-1}.[14] Wang *et al.* loaded Cr_2O_3 and Fe_2O_3 onto the SBA15 molecular sieve by the impregnation method to prepare Cr_2O_3&Fe_2O_3@SBA15 (CFS) as a thermal catalyst for the effective removal of SF_6. The results showed that CFS achieved an SF_6 degradation capacity of up to 313.15 mL g^{-1} at 700 °C, with a degradation duration of more than 420 min, demonstrating excellent stability and durability.[15] The above studies demonstrated that transition metals and their compounds contribute to the catalytic conversion of SF_6. Mechanistically, transition metals have a variety of oxidation states and coordination numbers, and their d orbital electrons can participate in the electron transfer process of the reactants and help to break chemical bonds, thus reducing the reaction activation energy.[12,16] However, current studies of thermocatalytic degradation of SF_6 are usually conducted under an inert atmosphere such as argon or nitrogen, which is very different from the actual conditions under which leaking SF_6 is mixed with air.[17] Consequently, it remains a difficult challenge to find a catalyst for the efficient degradation of SF_6 under an air atmosphere.

Transition metal manganese-based catalysts have garnered significant attention due to their availability, low cost, and environmental friendliness.[18] Manganese monomers and manganese oxides, in particular, have shown good promise for various catalytic applications such as oxidation and reduction reactions.[19,20] Manganese has a variety of oxidation states (*e.g.*, Mn^0, Mn^{2+}, Mn^{3+}, and Mn^{4+}), which makes it suitable for use in redox reactions during SF_6 degradation.[21] Recent studies have shown that manganese-based catalysts have great potential for SF_6 decomposition.[22] However, a detailed understanding of their catalytic mechanism is still necessary.

Hence, this study investigated the effect of the electronic structure of manganese-based catalysts on their performance toward the degradation of SF_6, using manganese in different oxidation states (Mn, MnO, Mn_2O_3, and MnO_2) as the active center and silicon carbide (SiC) as the carrier. The results showed that the SiC–Mn(0) composite with manganese as the active center exhibited the best degradation performance, with a degradation capacity of 62.27 mL g^{-1} at 600 °C. In addition, the degradation activity of the manganese-based catalysts for SF_6 decreased with increasing oxidation state of the elemental manganese. This indicated that the reducibility of the catalyst played a crucial role in the catalytic reduction of SF_6.

2. Experimental

2.1. Chemicals

Manganese (Mn), manganese oxide (MnO), manganese sesquioxide (Mn_2O_3), manganese dioxide (MnO_2), silicon carbide (SiC), rectorite, silicon dioxide (SiO_2), phosphorus pentoxide, boron trioxide, sodium hydroxide and anhydrous ethanol were purchased from Shanghai Macklin Biochemical Technology Co., Ltd. The chemicals employed in this experiment have not undergone additional purification steps.

2.2. Synthesis of SiC–Mn

The SiC–Mn composites were synthesized using a manual mechanical mixing method. The SiC and Mn monomers were mixed in a 4 : 1 mass ratio, with a total weight of 2.5 g. The mixture was ground manually in an agate mortar with an agate pestle for 10 minutes to ensure thorough mixing. The grinding was performed using a rotary motion with moderate pressure to ensure intimate contact between the SiC and Mn particles.

2.3. Synthesis of SiC–MnO(II), SiC–Mn_2O_3(III), and SiC–MnO_2(IV)

Under unchanged conditions that the total amount of the mixed sample is 2.5 g and the proportion of Mn atoms in the mixture is 20 wt%, changing the oxidation states of the Mn species, such as MnO, Mn_2O_3, and MnO_2, can lead to Mn-based catalytic materials, such as SiC–MnO(II), SiC–Mn_2O_3(III), and SiC–MnO_2(IV), with different active centers.

2.4. Materials characterization

The crystallographic properties of the samples were tested and analyzed using powder X-ray diffraction (PXRD) using a PXRD-6100 instrument (Shimadzu Co., Ltd, Japan), with Cu-Kα radiation source (λ = 0.154178 nm), and tube current and tube voltage set to 40 mA and 40 kV, respectively, at a scanning rate of 6° min^{-1}, and scanning angle range of 10°–65°. The micro-morphology of the samples was characterized using a Nova Nano SEM 450 model field emission scanning electron microscope (FE-SEM) with an accelerating voltage of 10 kV. Transmission electron microscopy (TEM), using an FEI Talos F200X model, was conducted to test and analyze the micromorphology and crystal spacing of the samples at an accelerating voltage of 200 kV.

2.5. SF_6 degradation testing

The degradation performance of the samples was analyzed using a heated reaction bed device, as shown in Fig. S1.† 2.5 g of the sample was placed into a glass tube with an inner diameter of 8 mm, blocked at both ends with quartz cotton, and then positioned in a tube furnace, and the temperature was set to 600 °C. The concentration of the SF_6 reaction gas was 3 vol% (ratio of SF_6 to air = 3 : 97), and the flow rate was 10 mL min^{-1}. At the end of the reaction, the acidic exhaust gas produced by the reaction was absorbed with 5 mol L^{-1} NaOH solution. The concentration of SF_6 in the tail gas was analyzed by gas chromatography. The SF_6 degradation capacity was calculated using eqn (1) as follows:

$$X_{SF_6} = \frac{[C_{SF_6}]_{in} - [C_{SF_6}]_{out}}{[C_{SF_6}]_{out}} \times 100\% \quad (1)$$

where $[C_{SF_6}]_{in}$ and $[C_{SF_6}]_{out}$ are the SF_6 concentrations in the inlet and outlet, respectively.

2.6. DFT calculations

Density functional theory (DFT) calculations were performed using plane-wave basis sets on Materials Studio version 2020.

In order to optimize Mn, MnO, Mn_2O_3 and MnO_2 crystal structures, the exchange-correlation function, PBE generalized gradient approximation with Koelling–Hamon relativistic treatment and spin polarization assumption were employed. The Broyden–Fletcher–Goldfarb–Shanno geometry optimization was used for cell optimization.[23] The interaction between valence electrons and the ionic core was described using the On-The-Fly-Generation ultrasoft pseudo potential.[24] The kinetic cutoff energy for the convergence test was set to 490 eV, while a *k*-point mesh (8 × 8 × 8) was applied for Brillouin zone sampling. The threshold for self-consistent field iterations was 2.0×10^{-6} eV per atom. The convergence tolerance parameters of the optimized calculations were defined as follows: an energy the tolerance of 2.0×10^{-5} eV per atom, a maximum force of 0.05 eV $Å^{-1}$, and a maximum displacement of 2×10^{-3} Å.

3. Results and discussion

To comprehensively investigate the crystalline structure of the catalysts, XRD analysis was conducted on four composite materials, with the results being presented in Fig. 1. The diffraction peaks observed at 2θ = 34.1°, 35.6°, 38.1°, 41.4°, 54.6°, and 60.0° corresponded to the (101), (006), (103), (104), (107), and (108) crystal planes of SiC, respectively.[25] In Fig. 1a, the diffraction peaks at 2θ = 43.0° and 47.8° could be precisely attributed to the Mn monolithic crystal phase, consistent with JCPDS no. 71-4929.[26] For the SiC–MnO composite, shown in Fig. 1b, characteristic MnO peaks were observed at 2θ = 34.9° (corresponding to the (111) plane), 40.5° (corresponding to the (200) plane), and 58.8° (corresponding to the (222) plane).[27] The PXRD pattern of the SiC–Mn_2O_3 composite revealed distinct diffraction peaks at 2θ values of approximately 23.1°, 32.9°, 38.2°, and 55.3°, which were indicative of the Mn_2O_3 phase, corresponding to the (222), (400), (332), and (440) planes, respectively.[28] Lastly, in Fig. 1d, the peaks observed at 2θ values of 37.1°, 42.4°, 56.0°, and 66.8° were associated with MnO_2, corresponding to the (100), (101), (102), and (110) crystal planes, respectively.[29] These PXRD results collectively confirmed the successful synthesis of the four composite materials, each exhibiting the expected crystallographic characteristics of both SiC and the respective manganese oxide phases.

Fig. 2 illustrates the SEM images of the four composites (SiC–Mn, SiC–MnO, SiC–Mn_2O_3 and SiC–MnO_2), revealing their surface morphology and microstructural features. For the SiC–Mn composite (Fig. 2a and b), the SEM images demonstrated that SiC exhibited a more disordered block structure with a particle size distribution that was not completely uniform, and smaller-sized Mn monolithic particles with a relatively uniform distribution could be found in the vicinity of the SiC blocks, suggesting that the manganese phase was effectively bonded to the SiC framework. In the SiC–MnO com-

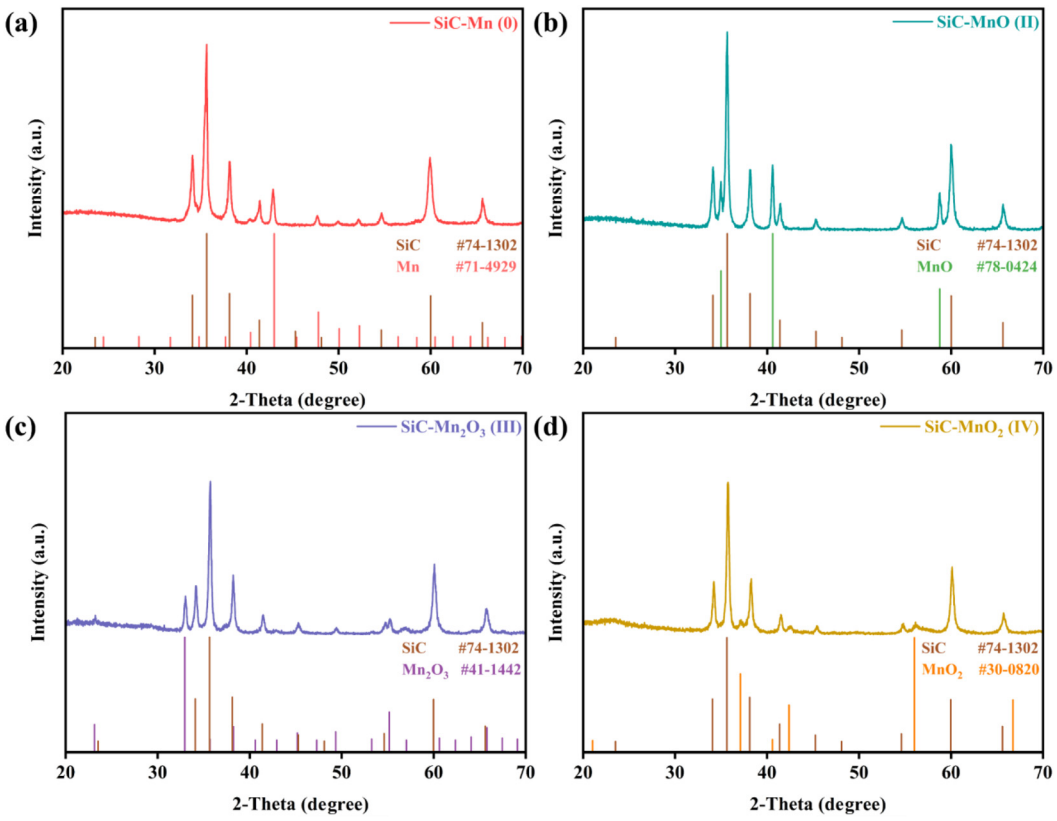

Fig. 1 PXRD patterns of (a) SiC–Mn, (b) SiC–MnO(II), (c) SiC–Mn_2O_3(III), and (d) SiC–MnO_2(IV).

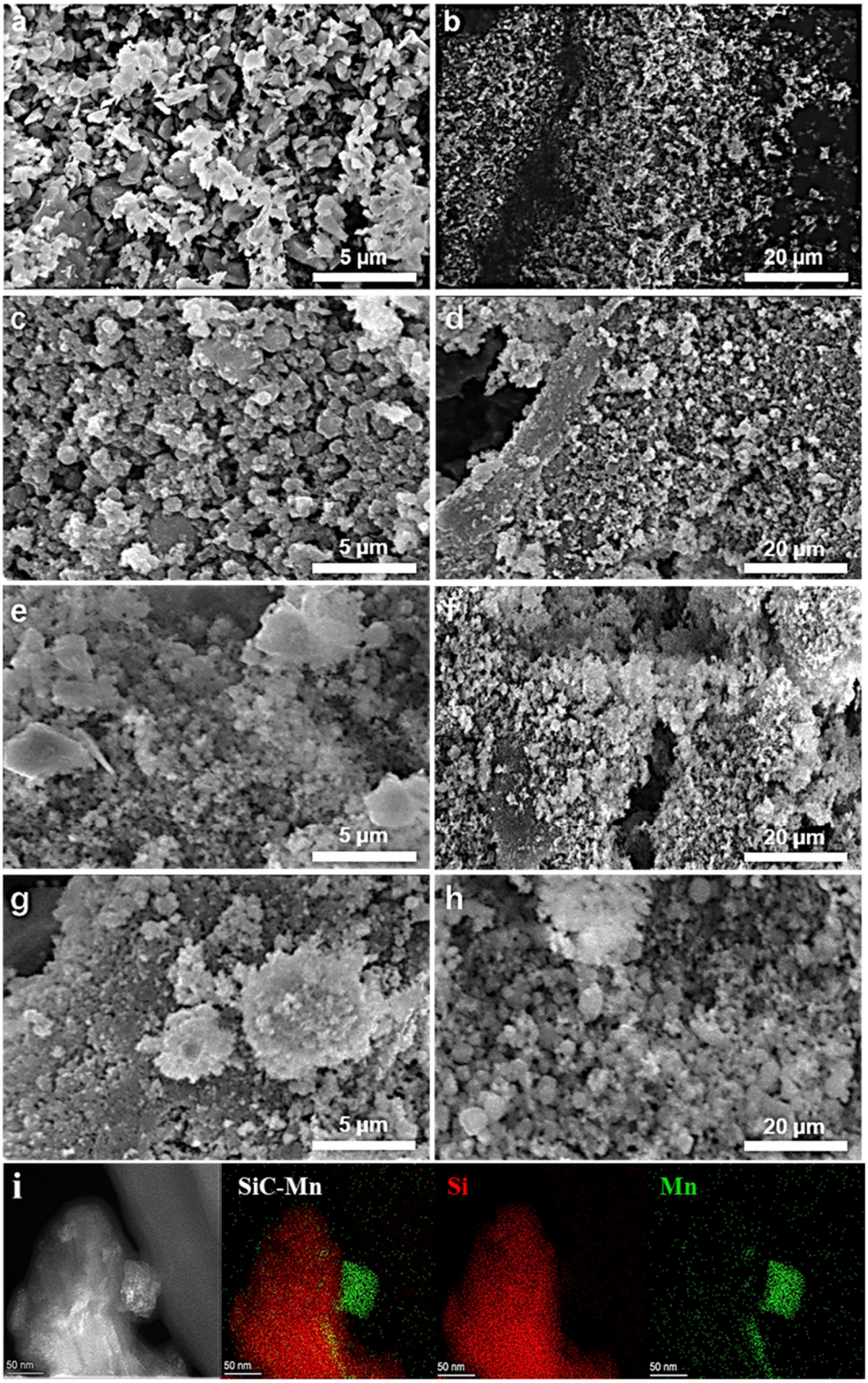

Fig. 2 SEM images of the composites (a and b) SiC–Mn(0), (c and d) SiC–MnO(II), (e and f) SiC–Mn_2O_3(III) and (g and h) SiC–MnO_2(IV), and (i) TEM mapping images of SiC–Mn(0).

posite (Fig. 2c and d), the SEM images revealed the formation of well-defined MnO particles in the SiC matrix. These particles showed a porous structure with a particle size of roughly 1 μm (Fig. S3a†), indicating a certain degree of porosity at the MnO–SiC interface, which may increase the surface area of the composite and thus improve its catalytic efficiency. The SEM analysis of the SiC–Mn_2O_3 composite (Fig. 2e and f) highlighted the lumpy nature of Mn_2O_3 with non-uniform particle

size distributions and the presence of significant agglomerations as compared to SiC–Mn and SiC–MnO composites, and the presence of these clusters may affect the overall surface area and reactivity of the composites. Lastly, the SiC–MnO_2 composite (Fig. 2g and h) showed a unique microstructure, in which the MnO_2 phase presents a spherical structure dispersed throughout the SiC matrix. However, most of the manganese dioxide particles were clustered together. In addition, the elemental distribution of SiC/Mn composites was observed under TEM, as shown in Fig. 2i. The SiC/Mn composites were characterized by the presence of the SiC carrier, and the Mn monomer. Among them, the Mn elements in the green signals represented the Mn monomers, and the Si elements in the red signals represented the SiC carriers, which visually proved that SiC and manganese elements were successfully combined.

The distribution and continuous supply of electrons in the composites were found to exert significant influence on the catalytic degradation of SF_6.[30] Therefore, the effects of active centers of Mn species with different oxidation states and different electron supply capacities on SF_6 degradation were investigated using SiC as a carrier, as shown in Fig. 3a. Among the four composites, the SiC–Mn(0) material exhibited the highest SF_6 degradation rate, which reached 98.8% at 600 °C while the degradation lifetime reached 180 min. This excellent performance can be attributed to the fact that the Mn monomers present in the reduced state promote efficient activation of the SF_6 molecules and the large surface area provided by the SiC substrate combined with the active Mn centers produces an efficient catalytic process. The SF_6 degradation efficiency of the SiC–MnO composites was slightly lower compared to that of SiC–Mn, with the highest degradation rate close to 95.3% after 40 min of reaction, which was attributed to the SiC matrix structure and the dispersion of the MnO clusters, both of which provided accessible active sites for SF_6 adsorption and activation. The degradation performance of SiC–Mn_2O_3 composites was significantly lower than that of SiC–Mn and SiC–MnO composites, with the highest degradation rate of 43.2% and degradation duration of 100 min. The Mn_2O_3, which was mainly in the oxidation state of Mn(III), hindered the electron transfer process necessary for the degradation reaction of SF_6 molecules, resulting in a significant decrease in the catalytic performance.[30] In addition, the blocky and dense Mn_2O_3 particles may also influence the overall reaction by potentially reducing the exposure of active sites to SF_6 molecules. For SiC–MnO_2 composites, limited degradation rates were exhibited starting after 20 min of reaction at a constant temperature, with the highest degradation rate of 14.3% at 40 min, followed by a rapid and complete loss of degradation activity by 80 min. Although MnO_2, characterized by the Mn(IV) oxidation state, has a relatively high oxidation potential, it is unable to activate the highly stable SF_6 molecule. The efficiencies per unit mass of the four samples in SF_6 degradation were subsequently calculated (Fig. 3b). The efficiency of SiC–Mn for SF_6 degradation at 600 °C was 62.27 mL g^{-1}, which was 1.6 and 4.2 times higher than that of SiC–MnO and SiC–Mn_2O_3, respectively, indicating that the different oxidations states of Mn play a key role in determining the catalytic efficiency.

As shown in Fig. 4, the four reacted Mn-based composites were analyzed using PXRD after the thermocatalytic degradation of SF_6. The results showed that the formation of $MnSiO_3$ (JCPDS #12-0181) was clearly observed in all three composites, SiC–Mn(0), SiC–MnO(II) and SiC–Mn_2O_3(III).[31] Among the four materials, the SiC–Mn composite showed the most pronounced $MnSiO_3$ diffraction peaks, particularly at 2θ = 29.4°, 32.1°, 51.5° and 58.3°, which corresponded to the (210), (221), (101) and (111) crystal planes of $MnSiO_3$, respectively (Fig. 4a).[32] This result was consistent with the excellent catalytic performance of this composite, suggesting a higher degree of interaction between the active Mn sites and the SF_6 molecules, which led to a significant structural transformation. Diffraction peaks of $MnSiO_3$ were also observed in the reacted SiC–MnO and SiC–Mn_2O_3 composites (Fig. 4b and c), which suggested that MnO and Mn_2O_3 were involved in the reaction with SF_6, but Mn in its oxidized states was less reactive toward SF_6. In addition, it is worth noting that peaks of

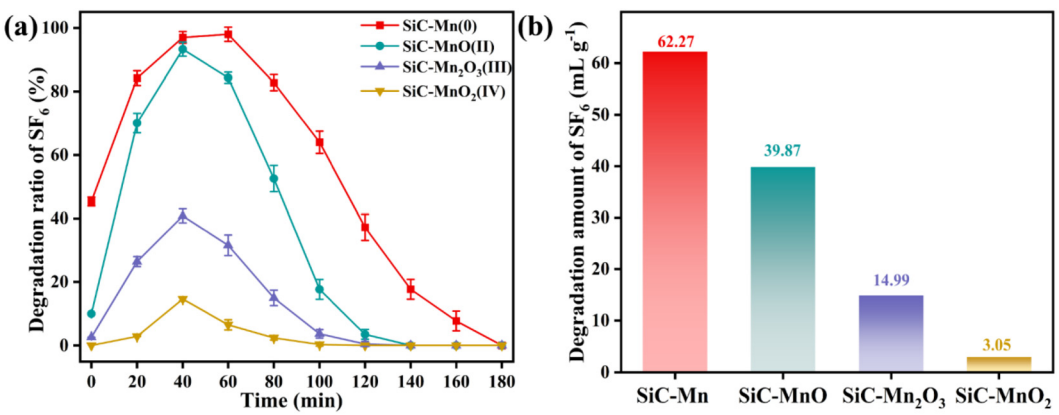

Fig. 3 Performance of SiC–Mn, SiC–MnO(II), SiC–Mn_2O_3(III), and SiC–MnO_2(IV) composites in the degradation of SF_6 from 0 to 180 min (a) and their final degradation capacity values (b).

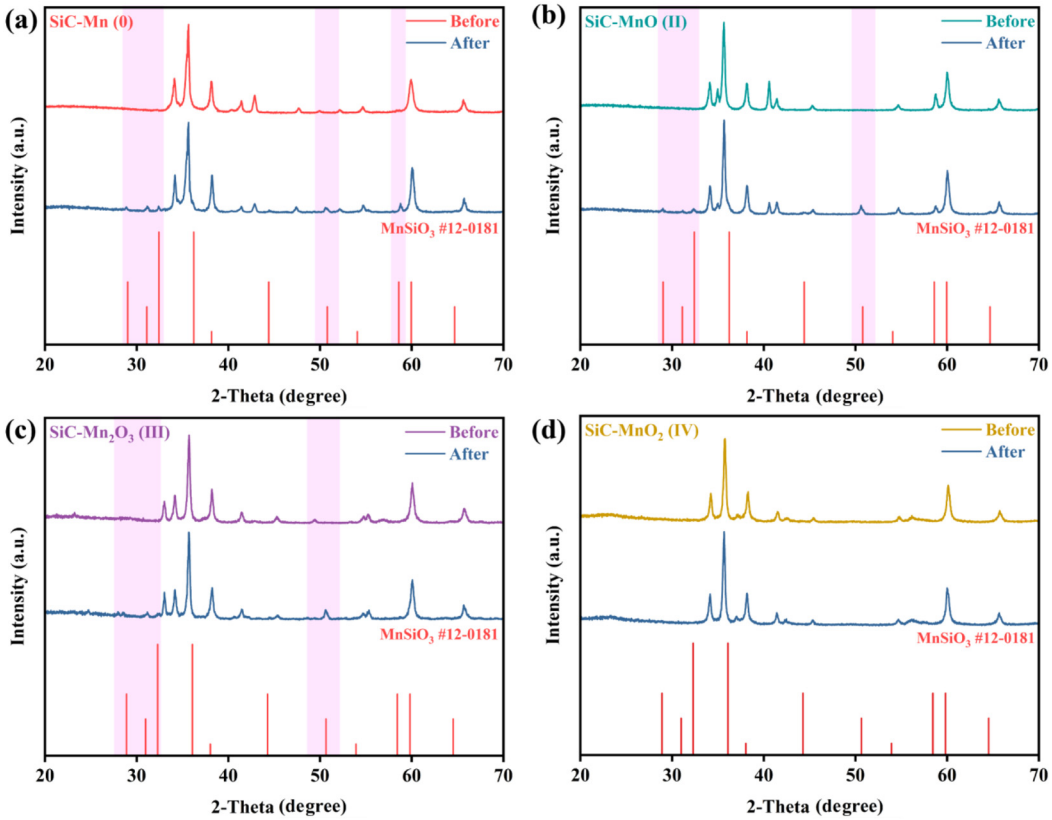

Fig. 4 PXRD patterns of (a) SiC–Mn(0), (b) SiC–MnO(II), (c) SiC–Mn_2O_3(III), and (d) SiC–MnO_2(IV) composites before and after the SF_6 degradation reaction.

strong MnO and Mn_2O_3 active phases are still visible in the patterns of reacted samples, but at this point, the samples have lost their degradation activity. This may be due to the fact that the $MnSiO_3$ covering the surface of the sample affects the expression of the properties of the internal MnO activity centers, whereas the metal silicates, such as $MnSiO_3$, have almost no activity in the degradation of SF_6. In the PXRD pattern of SiC–MnO_2 composite (Fig. 4d), the $MnSiO_3$ peak is barely detectable, which is consistent with the previously mentioned lack of catalytic activity of the SiC–MnO_2 composite. The PXRD spectra show that the SiC–MnO_2 composite remains essentially unchanged without substantial structural transformations or formation of secondary phases, which confirms its SF_6 degradation inactivity.

Carrier materials play an important role in the catalytic degradation of SF_6. The effect of various carriers on the thermocatalytic degradation of SF_6 was evaluated by complexing manganese monomers with several different carriers, including SiC, rectorite, SiO_2, B-doped SiC, and P-doped SiC, and the results are shown in Fig. 5a. Among the tested carriers, SiC was the most effective, with the highest SF_6 degradation rate, which was close to 100%, and a high degradation capacity of 62.27 mL g^{-1} over a reaction time of 180 min (Fig. 5b). This superior performance underscored the exceptional catalytic synergy between Mn and the SiC matrix, likely due to the large surface area and chemical compatibility of SiC, which facilitated the activation and breakdown of SF_6 molecules. In addition, rectorite–Mn composites using layered silicate clays as carriers showed some degradation activity, but their performance was relatively low with a degradation capacity of only 24.67 mL g^{-1}. In contrast, when Mn was composited with SiO_2, a commonly used carrier for supported catalysts, the resulting SiO_2–Mn composite exhibited virtually no degradation effect on SF_6. This finding suggests that the carrier in supported catalysts not only stabilized the active phase, but also actively participated in the catalytic reaction, enhancing or in some cases hindering the overall performance of the catalyst. Additionally, we investigated the impact of surface modification of SiC by doping it with boron and phosphorus. SEM mapping indicated that the distribution of B and P was relatively uniform (Fig. S4†). The B-doped and P-doped SiC–Mn composites displayed significantly reduced degradation performance, achieving a degradation capacity of only 13.48 mL g^{-1} and 34.22 mL g^{-1}, respectively, while the degradation duration extended only to approximately 120 min. The inferior performance of the doped SiC composites could be attributed to alterations in the surface morphology and chemical composition induced by doping, which likely disrupted the optimal interaction between the Mn active sites and the SiC carrier.[33]

To further explore the electron density distribution of the crystal structures of Mn, MnO, Mn_2O_3 and MnO_2, the Mulliken

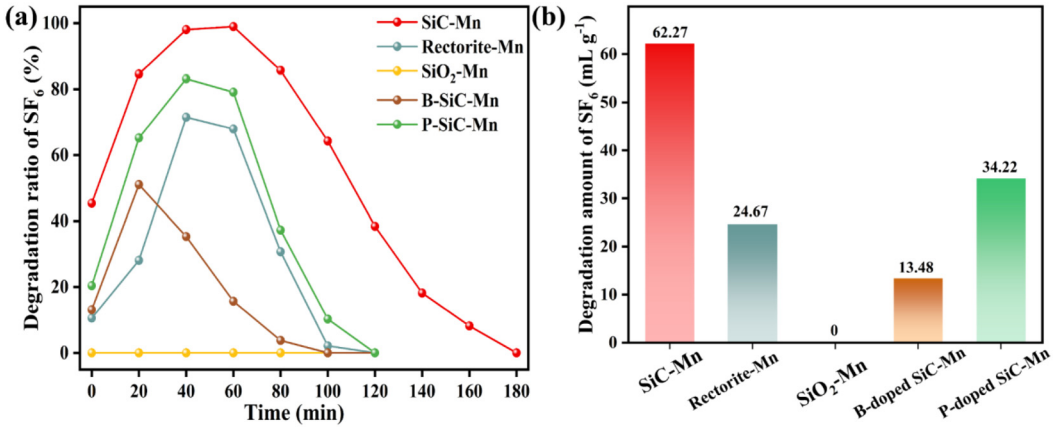

Fig. 5 The effect of the carrier material of different Mn composites on SF_6 degradation performance (a) and their final degradation capacity values (b).

charges of manganese atoms in the four materials were analyzed using DFT calculations. The calculation results (Fig. 6) show that the Mn monomers have the lowest value of Mulliken charge (+0.23*e*), indicating the weakest positive charge density distribution with a high proportion of delocalized free electrons in the crystal lattice; in contrast, the Mulliken charge of Mn atoms increases with the oxidation state to +1.39*e*, +1.59*e*, and +1.69*e* in turn, indicating enhanced electron depletion and reduced electron-donating capacity as the oxidation intensifies. This charge distribution trend directly explains the significant advantage of SiC–Mn in the SF_6 degradation reaction: its electron-rich property can efficiently drive the electron transfer to the strongly stable SF_6 molecule to promote S–F bond breakage, whereas manganese oxides with high oxidation states (in particular SiC–MnO_2) participate in the reduction reaction with difficulty due to their insufficient electron density. Therefore, the SiC–Mn composite based on Mn metal exhibits far more activity in SF_6 degradation than its oxides.

The study revealed a clear relationship between the oxidation states of Mn in SiC–Mn-based composites and their effectiveness in degrading SF_6. As shown in Fig. 7, SiC–Mn(0) composites, in which Mn was in the elemental form Mn^0, showed the strongest ability in the degradation of SF_6, with a

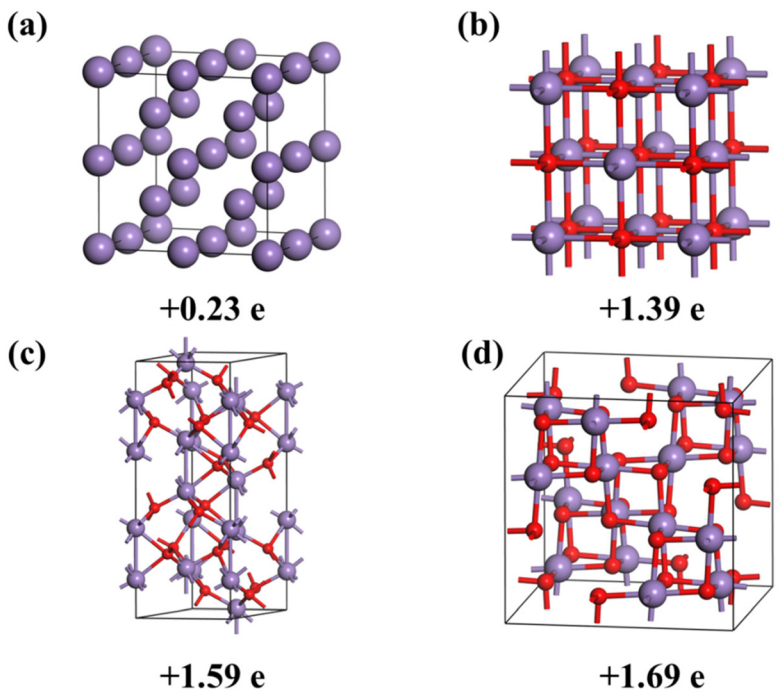

Fig. 6 Crystal structure diagrams and Mulliken charge values of Mn atoms in (a) Mn, (b) MnO, (c) Mn_2O_3 and (d) MnO_2 lattices.

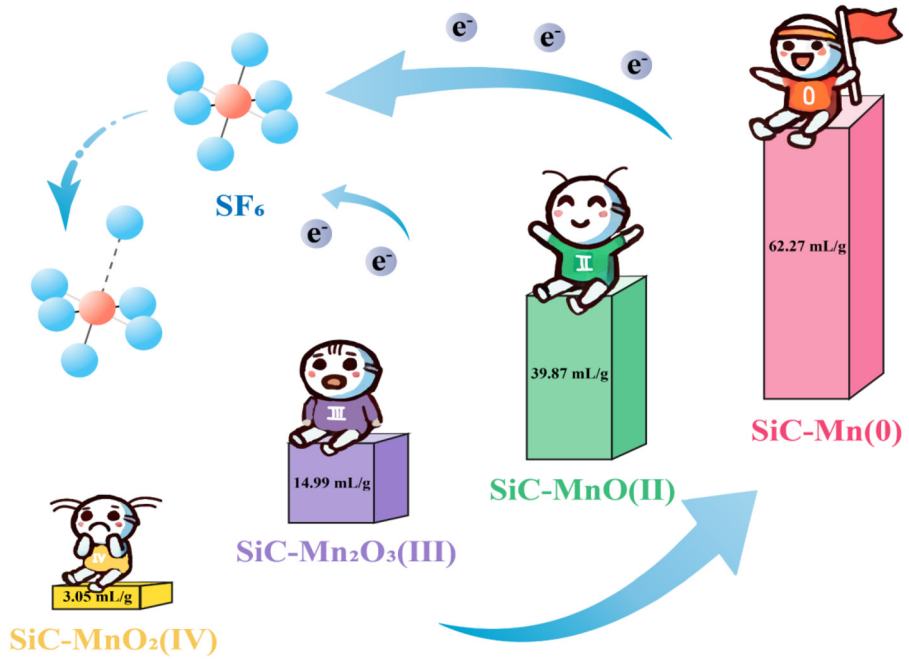

Fig. 7 SF_6 degradation performance of Mn-based catalysts with Mn in different oxidation states.

maximum degradation capacity of 62.27 mL g^{-1} at 600 °C. The degradation trend followed a clear order: SiC–Mn(0) > SiC–MnO (II) > SiC–Mn_2O_3(III) > SiC–MnO_2(IV), suggesting that catalytic activity decreases with increasing Mn oxidation state. As the oxidation state of Mn increases, its reducibility decreases. In the context of SF_6 degradation, which is a highly reducing process, the ability of the catalyst to donate electrons played a crucial role in the mechanism.[34] SF_6 is a kinetically stable molecule, which requires significant energy to break its bonds.[35] A reducing catalyst with a strong electron-donating capacity can effectively facilitate the cleavage of these bonds by providing the necessary electrons.[36] As the oxidation state of Mn increases, as seen in the SiC–MnO(II), SiC–Mn_2O_3(III), and SiC–MnO_2(IV) composites, the ability of Mn to donate electrons diminishes. This reduced electron-donating capability weakens the interaction between the catalyst and the SF_6 molecules, resulting in less efficient bond cleavage and, consequently, diminished degradation performance. The Mn(IV) valency state in SiC–MnO_2, in particular, was highly oxidized and lacked the necessary reductive power to effectively engage in the electron transfer required for SF_6 degradation, explaining the almost negligible catalytic activity observed for this composite.

4. Conclusions

In summary, we systematically investigated a series of Mn-based composites with potential for degrading SF_6 molecules. The results showed that the efficiency of Mn-based catalysts in the degradation of SF_6 was intrinsically linked to the oxidation state of the Mn active center. Composites with Mn in lower oxidation states, such as Mn(0) in SiC–Mn, exhibited the highest SF_6 degradation capacity of up to 62.27 mL g^{-1} at 600 °C, due to their excellent electron-carrying capacity, which provided the optimal conditions for bond cleavage in SF_6. The present study demonstrates the importance of selecting transition metal species with lower valency to maximize catalytic efficiency in the reduction of the SF_6 system.

Author contributions

Yaru Zhang: conceptualization and writing – original draft. Xiang Meng: conceptualization, resources, and writing – review & editing. Boxu Dong: resources. Fengxiang Ma: resources. Yue Zhao: resources. Xinhua He: supervision and writing – review & editing. Shan Zhu: supervision and writing – review & editing. Jiantao Zai: supervision and writing – review & editing.

Data availability

The authors declare that the data supporting the findings of this study are available within the paper and its ESI.† Should any raw data files be needed in another format they are available from the corresponding author upon reasonable request.

Conflicts of interest

The authors declare that they have no known competing financial interests or personal relationships that could have appeared to influence the work reported in this paper.

Acknowledgements

The authors are grateful for financial support from the Research and Application of Zero Emission Recovery Technology for sulfur hexafluoride based on catalytic degradation, and the Science and Technology Project of the State Grid Corporation of China (5200-202320487A-3-2-ZN)

References

1 S. Shi, Y. Li, Z. Cui, Y. Yan, X. Zhang, J. Tang and S. Xiao, *Chem. Eng. J.*, 2023, **470**, 144166.
2 H. Zhang, J.-X. Chen, J.-P. Qu and Y.-B. Kang, *Nature*, 2024, **635**, 610–617.
3 B. Zhao, Q. Xu and J. Lu, *Sci. Total Environ.*, 2024, **948**, 174992.
4 L. Guo and X. Fang, *Sci. Rep.*, 2024, **14**, 8753.
5 W.-T. Tsai and C.-H. Tsai, *Environments*, 2023, **10**, 113.
6 M. An, R. G. Prinn, L. M. Western, X. Zhao, B. Yao, J. Hu, A. L. Ganesan, J. Mühle, R. F. Weiss, P. B. Krummel, S. O'Doherty, D. Young and M. Rigby, *Nat. Commun.*, 2024, **15**, 1997.
7 L. Guo, Y. Yang, P. J. Fraser, G. J. M. Velders, Z. Liu, D. Cui, J. Quan, Z. Cai, B. Yao, J. Hu and X. Fang, *Commun. Earth Environ.*, 2023, **4**, 205.
8 C. Y. Chuah, Y. Lee and T.-H. Bae, *Chem. Eng. J.*, 2021, **404**, 126577.
9 W. Dong, Y. Zhao, F. Ma, F. Zhu, W. Liu, Y. Song, S. Zhu and H. Chen, *E3S Web Conf.*, 2023, **441**, 03012.
10 B. K. Sovacool, S. Griffiths, J. Kim and M. Bazilian, *Renewable Sustainable Energy Rev.*, 2021, **141**, 110759.
11 F. Zeng, R. Cai, C. Li, B. Xie, B. Deng, Q. Yao and J. Tang, *J. Phys. D:Appl. Phys.*, 2024, **57**, 135502.
12 P. Rotering, C. Mück-Lichtenfeld and F. Dielmann, *Green Chem.*, 2022, **24**, 8054–8061.
13 H. Li, F. Zeng, X. Guo, K. Zhu and J. Tang, *Sci. Total Environ.*, 2024, **931**, 172921.
14 J. Zhang, J. Z. Zhou, Z. P. Xu, Y. Li, T. Cao, J. Zhao, X. Ruan, Q. Liu and G. Qian, *Environ. Sci. Technol.*, 2014, **48**, 599–606.
15 J. Wu, J. Zhang, Z. Cao, Q. Liu, F. Wei, J. Zhou, D. Wang, S. Shi and G. Qian, *ACS Appl. Mater. Interfaces*, 2019, **11**, 16538–16545.
16 Y. Sun, G. Chen, S. Xi and Z. J. Xu, *ACS Catal.*, 2021, **11**, 13947–13954.
17 S. Zhu, Y. Zhao, F. Ma, Y. Yin, W. Shi, F. Zhu, W. Fan, P. Du and J. Ding, *Sustainable Energy Fuels*, 2024, **8**, 1918–1923.
18 C. Peng, D. Yu, L. Wang, X. Yu and Z. Zhao, *J. Mater. Chem. A*, 2021, **9**, 12947–12980.
19 R. Jamatia, A. Mondal and D. Srimani, *Adv. Synth. Catal.*, 2021, **363**, 2969–2995.
20 F. Wang, J. Deng, S. Impeng, Y. Shen, T. Yan, G. Chen, L. Shi and D. Zhang, *Chem. Eng. J.*, 2020, **396**, 125192.
21 X.-T. Huang, Y.-J. Sun, F. Zhang, C.-W. Bai and F. Chen, *Sep. Purif. Technol.*, 2024, **351**, 127837.
22 X. Meng, B. Dong, L. Zhao, W. Zhou, X. Li, J. Zai and X. Qian, *Appl. Catal., B*, 2024, **346**, 123709.
23 S. L. Dudarev, G. A. Botton, S. Y. Savrasov, C. J. Humphreys and A. P. Sutton, *Phys. Rev. B:Condens. Matter Mater. Phys.*, 1998, **57**, 1505–1509.
24 S. J. Clark, M. D. Segall, C. J. Pickard, P. J. Hasnip, M. I. J. Probert, K. Refson and M. C. Payne, *Z. Kristallogr. – Cryst. Mater.*, 2005, **220**, 567–570.
25 X. Zhao, W. Wu, D. Drummer, Y. Wang, S. Cui, C. Liu, Z. Lu, S. Li and Q. Chen, *ACS Appl. Electron. Mater.*, 2023, **5**, 2548–2557.
26 Y. Zeng, B. Gaskey, E. Benn, I. McCue, G. Greenidge, K. Livi, X. Zhang, J. Jiang and J. Elebacher, *Acta Mater.*, 2019, **171**, 8–17.
27 O. Pech and S. Maensiri, *J. Alloys Compd.*, 2019, **781**, 541–552.
28 D. Wang, H. Li, N. Dong and S. Hui, *J. Environ. Eng.*, 2021, **147**, 04021039.
29 Y. Yang, Y. Wang, X. Li, C. Xue, Z. Dang, L. Zhang and X. Yi, *Environ. Pollut.*, 2022, **315**, 120218.
30 X. Zhang, X. Li, Y. Wang, F. Meng, Y. Zou, S. Tian and Z. Cui, *J. Electron. Eng. Technol.*, 2023, **18**, 1251–1262.
31 J. Wang, F. Wang, Z. Guan, J. Wei, Y. Tao, L. Li, S. Ma, S. Wu, Y. Pang, Z. Shen and H. Chen, *Electrochim. Acta*, 2023, **472**, 143428.
32 J. Ye, K. Zhang, X. Yang, M. Liu, Y. Cui, Y. Li, C. Li, S. Liu, Y. Lu, Z. Zhang, N. Niu, L. Chen, Y. Fu and J. Xu, *Adv. Sci.*, 2024, **11**, 2307424.
33 C. Teng, Y. Chen, Z. Tang, W. Yuan, L. Zhang, Y. Guo, F. Li and Q. Huang, *Chem. Eng. J.*, 2024, **488**, 150983.
34 X. Meng, J. Hu, B. Dong, Y. Zhu, Y. Zhang, J. Zai and X. Qian, *Chem. Eng. J.*, 2022, **450**, 137949.
35 H. Li, F. Zeng, M. Zhang, K. Zhu, Q. Yao and J. Tang, *J. Phys. D:Appl. Phys.*, 2023, **56**, 445503.
36 M. Govindan, R. Adam Gopal and I. S. Moon, *Chem. Eng. J.*, 2020, **382**, 122881.